International Journal of Thermal Sciences 162 (2021) 106772

Contents lists available at ScienceDirect

International Journal of Thermal Sciences

journal homepage: http://www.elsevier.com/locate/ijts

Intrinsically low lattice thermal conductivity of monolayer hexagonal aluminum nitride (*h*-AlN) from first-principles: A comparative study with graphene

Huimin Wang [a,b,c], Linfeng Yu [b], Jinyuan Xu [b], Donghai Wei [b], Guangzhao Qin [b,*], Yagang Yao [a,d,**], Ming Hu [c,***]

[a] College of Engineering and Applied Science, Nanjing University, Nanjing, 210023, China
[b] State Key Laboratory of Advanced Design and Manufacturing for Vehicle Body, College of Mechanical and Vehicle Engineering, Hunan University, Changsha, 410082, PR China
[c] Department of Mechanical Engineering, University of South Carolina, Columbia, SC, 29208, USA
[d] Division of Nanomaterials, Suzhou Institute of Nano-Tech and Nano-Bionics, Nanchang, Chinese Academy of Sciences, Nanchang 330200, China

ARTICLE INFO

Keywords:
Monolayer III-V compound
Thermal conductivity
Phonon transport
Electronic structure
First-principles

ABSTRACT

Stimulated by the research progress of graphene, lots of more graphene-like two-dimensional (2D) materials are well-explored in both theoretical and experimental studies for the potential applications in electronics, where high-performance thermal management plays a key role. In this paper, we performed the state-of-art first-principles study on the thermal transport properties of monolayer *h*-AlN, which is a typical graphene-like 2D III-V compound with planar honeycomb structure and excellent electronic properties. It is found that *h*-AlN possesses a much lower thermal conductivity (73.43 W/mK at 300 K) compared to graphene (3094.98 W/mK). Detailed comparative analysis is presented in terms of mode level group velocity, scattering phase space (channel), and phonon anharmonicity. Furthermore, the electronic structures of *h*-AlN reveal the existence of isolated electron pairs, which play a key role in enhancing the orbit-driven strong anharmonicity and leading to the low thermal conductivity. The in-depth analysis of the low thermal conductivity of *h*-AlN sheds a light on future studies of thermal management materials.

1. Introduction

For many years, Two-dimensional (2D) materials have been intensively studied for its potential applications in nanoelectronics, which is one of the leading topics in condensed matter physics and materials science [1–5]. Stimulated by the research and development of graphene [6,7], lots of other graphene-like 2D materials are well-explored in both theoretical and experimental fields, such as semiconductor monolayer (ML) transition-metal dichalcogenides (TMDCs) [8], boron nitride (BN) [9,10], zinc oxide (ZnO) [11], *etc.*, which provide alternative solutions to the nanoelectronics overcoming the gapless feature of graphene. In particular, hexagonal boron nitride (*h*-BN), a novel 2D electrically insulating thermal conductor [9,10], can be used as an excellent dielectric substrate for graphene based electronics [12]. Besides, the wide band gap of ML *h*-BN (~5.0–6.0 eV) further establishes the key role of 2D nitrides in promoting the development of next generation nanoelectronics, which inspires researchers to pay more attention to the 2D nitrides beyond *h*-BN.

Hexagonal aluminum nitride (*h*-AlN), a kind of analogue of *h*-BN, is a typical 2D nitride with the semiconductor feature, which has attracted lots attention for its wide applications in opto-electronics and energy engineering [13]. For instance, previous studies have shown theoretically that *h*-AlN possesses an indirect band gap of 2.81 eV and its structure is dynamically stable [13,14]. In addition to the theoretical studies, it has been also reported experimentally that the *h*-AlN can be obtained by epitaxial growth on various crystal substrates, such as Ag, SiN, *etc.* For instance, P. Tsipas *et al.* [15] reported that ultrathin (sub-monolayer to 12 layers) AlN nanosheets can be grown on Ag (111)

* Corresponding author.
** Corresponding author. College of Engineering and Applied Science, Nanjing University, Nanjing, 210023, China.
*** Corresponding author.
E-mail addresses: gzqin@hnu.edu.cn (G. Qin), ygyao2018@nju.edu.cn (Y. Yao), hu@sc.edu (M. Hu).

https://doi.org/10.1016/j.ijthermalsci.2020.106772
Received 18 July 2020; Received in revised form 12 November 2020; Accepted 26 November 2020
1290-0729/© 2020 Elsevier Masson SAS. All rights reserved.

single crystals by plasma assisted molecular beam epitaxy. Mansurov *et al.* [16] reported that AlN layers were formed by the deposition of Al onto SiN (8 × 8) surface.

It has been well realized that the high-efficient heat dissipation plays a key role because the accumulated thermal energy will lead to the decay of both lifetime and performance of modern micro and nano-electronics devices. Thus, high performance thermal management is becoming an important issue in the electronic industry [17]. For semiconductors, the phonon is the primary carrier for thermal transport. Thus, with the potential application in nanoelectronics and optoelectronics, the systematical study of the phonon transport properties of *h*-AlN is necessary, which will be of great significance to its broad applications. Furthermore, the thermal transport in *h*-AlN can be regulated by alloying with other 2D materials, which would promote the potential applications in broad fields. For instance, future studies can be conducted to explore the hybrid graphene [18] and *h*-AlN in different configurations and design multifunctional structures based on *h*-AlN for thermoelectrics [19,20]. For such studies, the machine learning methods could be powerful.

In this paper, the phonon transport properties of *h*-AlN are comprehensively studied by solving the Boltzmann transport equation (BTE) based on first-principles calculations. The thermal conductivity of monolayer *h*-AlN is calculated to be 74.43 W/mK at 300 K, which is about two orders of magnitude lower than that of graphene (3094.98 W/mK) despite their similar planar honeycomb structure. Such a low thermal conductivity makes monolayer *h*-AlN a promising candidate for achieving high thermoelectric performance in the field of thermal management such as rewriteable devices [21–23] and thermal barrier coatings [24,25].

The rest of the paper are organized as follows. In section 2, we described the calculation method of the first principle and the Boltzmann transport theory of phonon transport. In section 3.1 and 3.2, we discussed the similarities and differences of *h*-AlN and graphene in structure, phonon dispersion and phonon transport properties. Furthermore, the mode level analysis of the low thermal conductivity of *h*-AlN is presented in section 3.3, including the analysis of scattering processes and scattering channels. The size effect is discussed in section 3.4. Finally, based on the analysis of charge transfer and orbital hybridization, a deep understanding of the low thermal conductivity of *h*-AlN is illuminated. In section 4, summary and conclusions are given as end.

2. Computational methodology

All the first-principles calculations are performed based on density functional theory (DFT), using the Vienna *ab-initio* simulation package (VASP) [26–28]. Perdew-Burke-Ernzerhof (PBE) implementation of the generalized gradient approximation (GGA) is treated as exchange-correlation functional. The kinetic energy cutoff of wave function expanded in plane wave is about 2.5 times of the maximal recommended cutoff in the pseudo-potentials for the high precision. A large vacuum spacing (~20 Å) along the out-of-plane direction is used to avoid interactions caused by the periodic boundary conditions between layers. With 15 × 15 × 1 Monkhorst-Pack [29] *k*-point mesh used to sample in the first Brillouin zone (BZ), the geometry structures are fully relaxed until the maximal Hellmann-Feynman force is smaller than 1×10^{-7} eV/Å. Through diagonalizing the harmonic dynamical matrix, the phonon dispersions can be obtained by using Phonopy package [30] with the constructed 5 × 5 × 1 supercells based on the optimized structure. The harmonic and anharmonic interatomic force constants (IFCs) are calculated by the real-space finite displacement difference method. The cutoff radius is used in anharmonic IFCs' calculations to discard atomic interactions between atoms for practical purposes if their distance is larger than a certain value. Born effective charges and dielectric permittivity tensor calculated with the density functional perturbation theory (DFPT) are added to the dynamical matrix for correcting the long-range electrostatic interactions.

The thermal conductivity is obtained by solving phonon BTE as implemented in the ShengBTE package [31,32]. Phonons are the primary carriers of thermal transport, which are distributed obeying the Bose-Einstein function $f_0(\omega_\lambda)$ at thermal equilibrium due to the absence of temperature gradient ∇T or other thermodynamical forces [32]. At steady state, assuming the temperature gradient is small enough in most practical situations, the phonon distribution function f_λ can be linearized in ∇T as:

$$f_\lambda - f_0(\omega_\lambda) = -\boldsymbol{F}_\lambda \cdot \nabla T \frac{\mathrm{d}f_0}{\mathrm{d}T}, \tag{1}$$

where $\boldsymbol{F}_\lambda = \tau_\lambda^0(\nu_\lambda + \Delta_\lambda)$ when only three phonon scattering processes in considered [33–35]. In this case, the linear BTE is related to the phonon relaxation time τ, phonon group velocity υ and the measure of the deviation from relaxation time approximation (RTA). All the three-phonon scattering processes obey both energy and momentum conservation based on phonon dispersion:

$$\omega_j(\vec{q}) \pm \omega_{j'}(\vec{q'}) = \omega_{j''}(\vec{q''}), \quad \vec{q} \pm \vec{q'} = \vec{q''} + \vec{K}, \tag{2}$$

in which $\vec{K} = 0$ corresponds to Normal process, while $\vec{K} \neq 0$ corresponds to Umklapp process. The τ is inversely proportioned to phonon scattering rate, which can be divided into absorption and emission phonon processes:

$$\frac{1}{\tau_\lambda^0} = \frac{1}{N}\left(\sum_{\lambda'\lambda''}^{+} \Gamma^{+}_{\lambda\lambda'\lambda''} + \sum_{\lambda'\lambda''}^{-} \frac{1}{2}\Gamma^{-}_{\lambda\lambda'\lambda''} + \sum_{\lambda'} \Gamma_{\lambda\lambda'}\right), \tag{3}$$

where N is the number of discrete q points. $\Gamma^{+}_{\lambda\lambda'\lambda''}$, $\Gamma^{-}_{\lambda\lambda'\lambda''}$ and $\Gamma_{\lambda\lambda'}$ are the absorption scattering rate, emission scattering rate and isotopic disorder scattering rate, respectively. The κ can be obtained with the thickness of monolayer *h*-AlN and graphene being 3.1 and 3.4 Å, respectively.

3. Results

3.1. Structure and phonon dispersion

Monolayer *h*-AlN possesses the similar planar honeycomb structure with graphene, which belongs to the P$\bar{6}$m2 (No. 187) space group with 2 atoms per unit cell [Fig. 1]. The optimized lattice constants are 3.126 and 2.464 Å for monolayer *h*-AlN and graphene, respectively. The Al–N

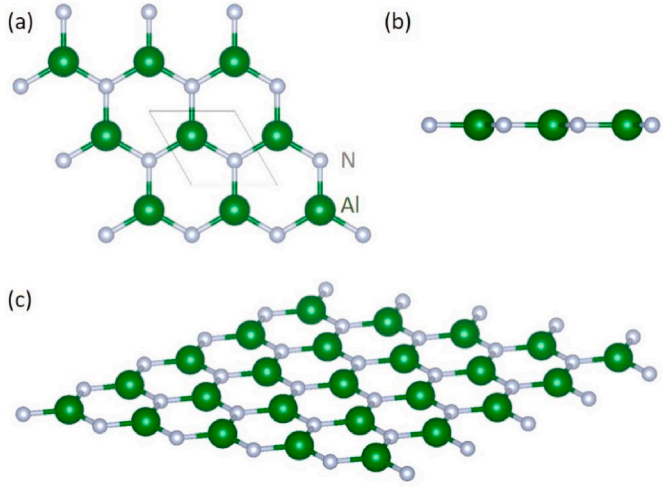

Fig. 1. The (a) top, (b) side and (c) perspective views of the structure of monolayer *h*-AlN. The primitive cell is marked in (a) with the dot diamond and the types of atoms are marked onsite.

bong length of *h*-AlN is 1.8 Å, larger than the C–C bond in graphene (1.422 Å). Based on the optimized structure, the phonon dispersions and partial density of states (pDOS) are calculated for confirming the structural stability [Fig. 2(a)]. The lacking of imaginary frequency indicates that the structures are thermally dynamical stable. Like graphene, monolayer *h*-AlN also presents the typical feature of 2D materials with the quadratic behavior of the flexural acoustic (FA) phonon branch when approaching the BZ center (Γ point). All the phonon branches of *h*-AlN are obviously softened compared to that of graphene, suggesting the strong phonon anharmonicity of *h*-AlN [36]. Moreover, compared to the no-gap graphene, a wide phonon band gap exists in the phonon dispersion of *h*-AlN, which is due to the large difference of atomic masses between Al and N as revealed by the pDOS. The phonon band gap could have a significant influence on the acoustic-acoustic and acoustic-optical phonon scattering.

The Grüneisen parameter is usually used to describe the phonon anharmonicity by charactering the relationship between the change of phonon frequency and the change of lattice volume. As shown in Fig. 2 (b), the large magnitude difference in the Grüneisen parameter between *h*-AlN and graphene, especially for the FA phonon branch, indicates the strong phonon anharmonicity of *h*-AlN.

3.2. Thermal transport properties

The intrinsic lattice thermal conductivity (κ) of monolayer *h*-AlN with the temperature ranging from 200 to 800 K shown in Fig. 3(a) is calculated by solving the phonon BTE with the iterative method. The κ of *h*-AlN is obtained as 73.43 W/mK at 300 K. Compared with other monolayer III-V compounds as shown in Table 1, the thermal conductivity of *h*-AlN is one order of magnitude lower than that of *h*-BN (~849 W/mK) [37] and is on the same order of magnitude as *h*-GaN (~15 W/mK) [38]. The difference in thermal conductivity can be explained by the Slack's formula that is the larger the atomic mass, the lower thermal conductivity. Obviously, the thermal conductivity of *h*-AlN is two orders of magnitude lower than that of monolayer graphene (~3094.98 W/mK) despite their similar planar honeycomb structure, which cannot be explained by the intuitive atomic mass differences. Thus, much deeper physical mechanisms need to be further explored. Note that *Zhao et al.* have reported the κ of *h*-AlN to be 264.1 W/mK based on classical non-equilibrium molecular dynamics (NEMD) simulations [14]. Considering the difference in the calculation methods, the results reported in this study fill the gap by predicting the κ of *h*-AlN based on the state-of-art first-principles calculations. More importantly, the first-principles based phonon BTE method can describe the phonon-phonon scattering events without any artificial parameters, which avoids the accuracy distortion by the empirical potential used in MD.

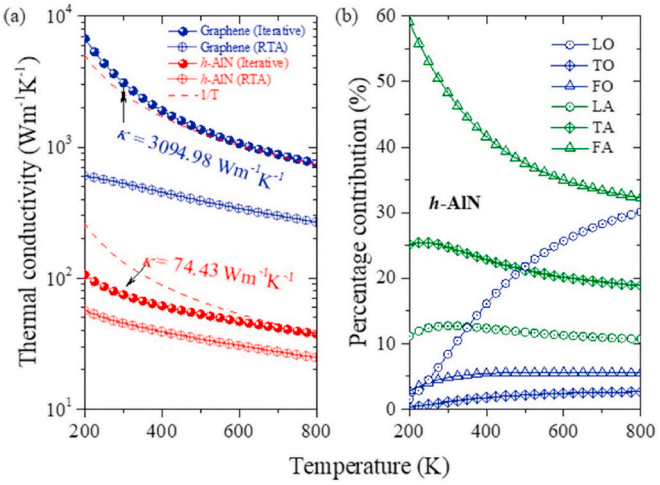

Fig. 3. (a) Temperature dependent lattice thermal conductivities of monolayer *h*-AlN and graphene calculated using iterative and RTA methods, respectively. The thermal conductivity of the $1/T$ law is plotted for comparison. (b) Temperature dependent percentage contribution to κ_L of each acoustic and optical phonon branch.

Table 1
Comparison of thermal conductivity at 300 K of III-V compound and graphene.

Type	Thermal conductivity (W/mK)	Methods	References
Graphene	3080–5150	Exp.	[7]
	3094.98 (this work)	First-principles	
h-BN	849	Exp.	[37]
	751	MD	[37]
Bulk AlN	321	Exp.	[39]
h-AlN	264.1	MD	[14]
	74.43 (this work)	First-principles	
h-GaN	37	First-principles	[44]
	14.93	First-principles	[38]

Commonly, the temperature-dependence behavior of 2D materials obeys the $1/T$ law such as graphene, silicene, phosphorene, *etc.* [38–41] However, the temperature dependence of the thermal conductivity of monolayer *h*-AlN between 200 and 500 K shows an slightly anomalous behavior [Fig. 3(a)], which is similar to that found in *h*-GaN [38]. Furthermore, we use the RTA method to calculate the thermal conductivity of *h*-AlN and the results are also shown in Fig. 3(a). It was found that the RTA underestimates the κ of *h*-AlN by 40.3% compared to the

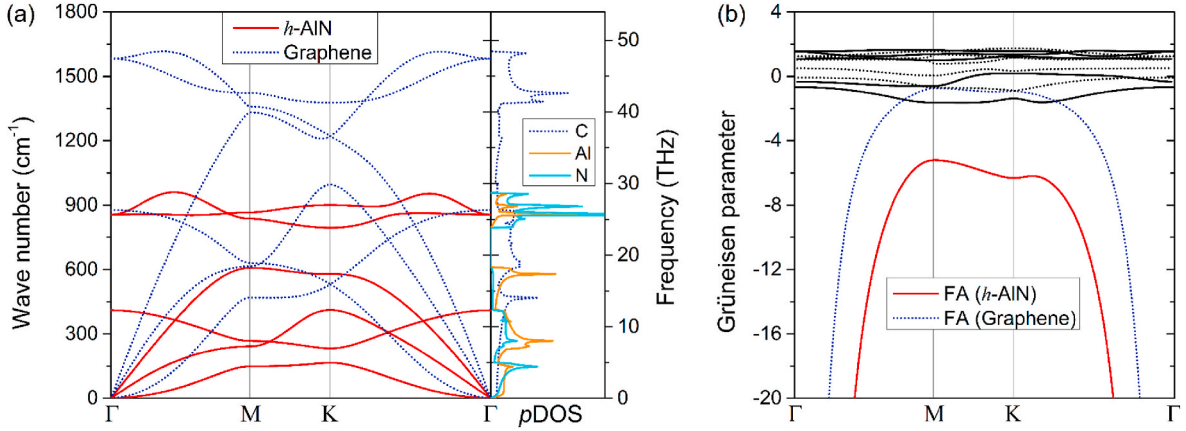

Fig. 2. Comparison of (a) phonon dispersion curves along the path passing through the high-symmetry *k*-points in the irreducible Brillouin zone, partial density of states (*p*DOS) and (b) Grüneisen parameters between *h*-AlN and Graphene.

accurate results from the iterative method. The underestimation of the RTA method is due to its treatment of the Normal process as thermal resistance while, in fact, the Normal process doesn't contribute thermal resistance [42]. Note that the underestimation is much less than that in graphene (83.2%) [40], indicating the dominating role of the Umklapp process in the phonon-phonon scattering for monolayer *h*-AlN.

To further explore the mechanism of low thermal conductivity of *h*-AlN and the anomalous temperature-dependent behavior, the temperature-dependent percentage contribution to κ of each acoustic and optical phonon branch is extracted in Fig. 3(b). Generally, acoustic phonon branches dominate the thermal conductivity. The temperature-dependent percentage contribution of the phonon branches decrease in a relationship close to the $1/T$, especially for the FA branch. Consequently, the thermal conductivity obeys the well-known $1/T$ law. For instance, graphene is a typical 2D material dominated by FA branches and thus it has an obvious $1/T$ relationship [40]. The situation is different for *h*-AlN. As shown in Fig. 3(b), the FO, TO, TA and LA branches of *h*-AlN show a weak temperature-dependence behavior and the phonon branches that dominate the temperature-dependence behavior are FA and LO. Due to the rapid increase of LO branch percentage contribution in the temperature range of 200–500 K, it suppresses the $1/T$ law to a certain extent and thus makes the slight difference in the temperature-dependence behavior between graphene and *h*-AlN. Taking into account the dominant role of FA, the thermal conductivity of *h*-AlN decreases slightly slower than that of graphene, but it is still close to the $1/T$ relationship, which is different from the abnormal temperature-dependent behavior of ZnO and GaN [38,41].

Furthermore, Fig. 4(a) shows the comparison of frequency dependent mode level group velocity between *h*-AlN and graphene for detailed understanding on the thermal transport. The overall group velocity of *h*-AlN is much smaller than that of graphene, especially in the low frequency range, which is consistent with the phonon dispersions as shown in Fig. 2(a). The small group velocity of *h*-AlN is due to the softened low-frequency phonon modes, which directly leads to its low thermal conductivity. A slightly larger group velocity in the high frequency region is found in *h*-AlN [Fig. 4(a)], which is caused by LO-TO split due to polarization [38,41]. The large group velocity in the high frequency region well explains the large contribution from LO to the thermal conductivity of *h*-AlN.

3.3. Analysis of the scattering processes

Considering the conservation of energy, the phonon-phonon scattering can be split into absorption and emission processes. Due to the dominating role of the FA phonon branches in the thermal conductivity of graphene and *h*-AlN, we mainly focus on the low-frequency region where a large phase space [Fig. 4(b)] describing the possibility of phonon-phonon scattering is evidently observed. Commonly, it is difficult for low-frequency phonons to emit due to the low energy caused by the low frequency. Thus, the phonon scattering processes in the low-frequency range for graphene and *h*-AlN are mainly dominated by the absorption process.

The fundamental insight into the phonon scattering processes can be achieved by analyzing the phonon scattering channels, which quantify the specific scattering processes among different phonon branches. Go a step further for the mechanism underlying the lower κ of *h*-AlN compared to graphene, we go into the detailed scattering channels of FA phonon modes along Γ-M direction to achieve fundamental understanding, which is plotted in Fig. 5(a) for graphene and Fig. 5(b) for *h*-AlN, respectively. It is found that the scattering rates from FA phonon modes of both graphene and *h*-AlN mainly come from the absorption process ($\vec{q} + \vec{q'} = \vec{q''}$), which is consistent with the results as shown in Fig. 4(b). For graphene, only two scattering channels is found for the FA phonon branch, and other possible scattering channels of FA phonon modes considering the conservation of energy and momentum from Equ (2) are prohibited, *i.e.*, FA+FA→TA and FA+FA→LA. Different from graphene, some other extra narrow scattering channels are found in *h*-AlN, which involves odd numbers of FA phonon modes, such as FA+FO→FO. The difference in the scattering channels of FA between graphene and *h*-AlN stems from the slight difference in their planar structures, which can be explained by the symmetry-based selection rule of phonon-phonon scattering [42]. Based on the examination of potential energy under the symmetry operation of the perfectly smooth planar structure of graphene, the phonon scattering processes involving odd numbers of FA phonon modes are largely suppressed. The large suppression results in a low scattering rate that is equivalent to a large relaxation time, and eventually leads to the high thermal conductivity of graphene. Unlike graphene, the planar structure of *h*-AlN is not so smooth due to the huge difference in the atomic radius and mass of Al atoms and N atoms [Fig. 1], which somewhat destroys the reflection symmetry of *h*-AlN. Thus, extra scattering channels are not fully prohibited in *h*-AlN by the reflection symmetry, which involves odd numbers of FA phonon modes [Fig. 5(b)]. Consequently, the scattering rate of FA phonon mode in *h*-AlN is larger than that in graphene as revealed in Fig. 5(c), which is equivalent to a small relaxation time and eventually leads to the ultra-low thermal conductivity of *h*-AlN compared to graphene. In addition, a higher scattering rate of the high-frequency phonon modes than the low-frequency phonon modes means that both *h*-AlN and graphene are typical 2D materials where phonon transport is dominated by the acoustic phonon modes.

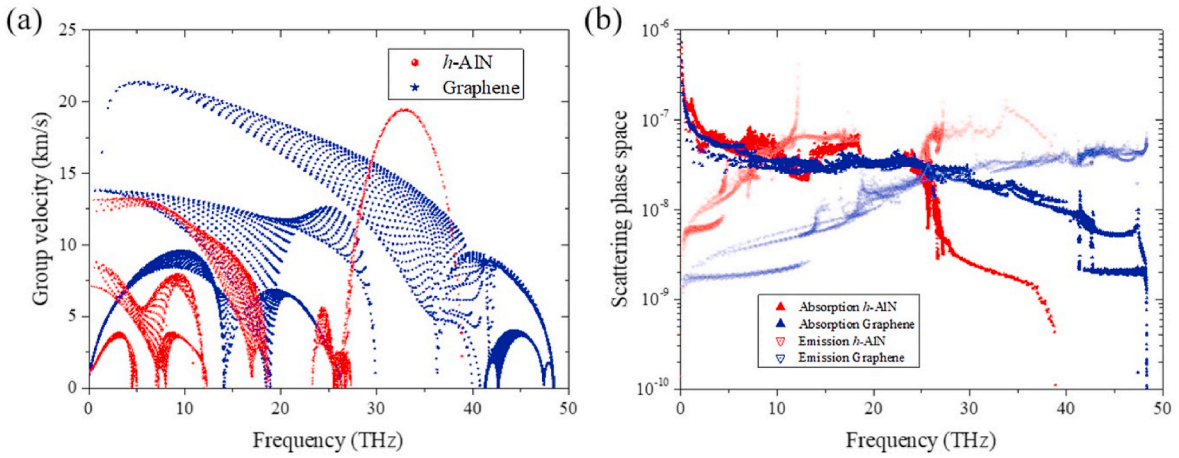

Fig. 4. Comparison of frequency dependent mode level (a) group velocity and (b) scattering phase space between graphene and *h*-AlN. Another version of the scattering phase space is provided in the supplementary material (Fig. S1).

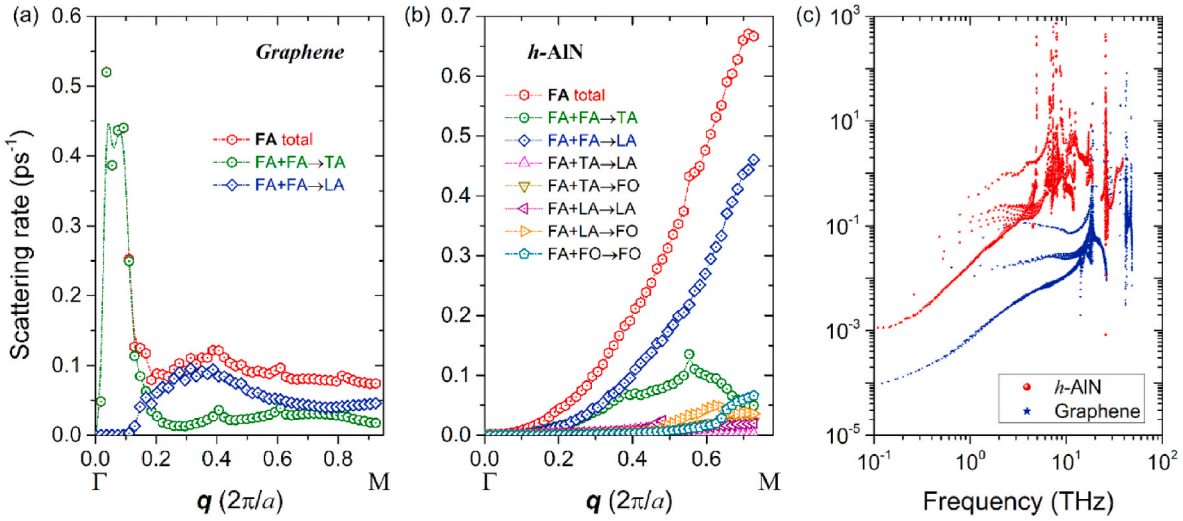

Fig. 5. Scattering channels of FA phonon modes along Γ-M direction for (a) graphene and (b) *h*-AlN. (c) The comparison of scattering rate between graphene and *h*-AlN.

Note that the specific heat capacity of *h*-AlN (2.047×10^6 J/(m^{3}K)) is much larger compared to graphene (1.570×10^6 J/(m^{3}K)), which compensates for the low contribution of *h*-AlN's low group velocity to thermal conductivity. Thus the two orders of magnitude lower κ of *h*-AlN than graphene [Fig. 3(a)] is mainly derived from the two orders of magnitude lower phonon lifetime (relaxation time) driven by the stronger phonon anharmonicity [Fig. 2(b)].

3.4. Size effect

At the micro-nano scale, the size effect has always been an important issue for designing nanostructures or nanodevices with desired thermal conductivity for the purpose of high-performance thermal management. To build an effective model, the mean free path, which demonstrates the size effect of phonon diffusive and ballistic transport, is discussed at two different representative temperatures of 300 and 800 K as shown in Fig. 6, respectively. Considering the phonon boundary scattering caused by the finite length of the material, the scattering rate can be calculated based on Matthiessen's rule [45]:

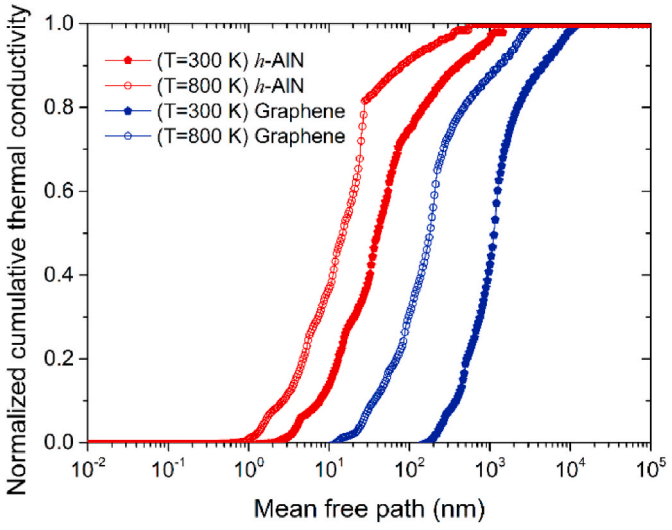

Fig. 6. Mean free path dependent normalized cumulative κ_L of graphene and *h*-AlN at 300 and 800 K, respectively.

$$\frac{1}{\tau(\vec{q},p)} = \frac{1}{\tau^{anh}(\vec{q},p)} + \frac{1}{\tau^{iso}(\vec{q},p)} + \frac{1}{\tau^{B}(\vec{q},p)}, \quad (4)$$

where $1/\tau^{anh}(\vec{q},p)$is the intrinsic anharmonic phonon-phonon scattering rates, $1/\tau^{iso}(\vec{q},p)$is the isotopic scattering rates, and $1/\tau^{B}(\vec{q},p)$ is the phonon-boundary scattering rates calculated by Ref. [45–47]:

$$\frac{1}{\tau^{B}(\vec{q},p)} = \frac{1-p}{1+p}\frac{|\nu_{\alpha}(\vec{q},p)|}{L}, \quad (5)$$

where L represents the characteristic size of the system which is regarded as the dimension of the width direction perpendicular to the infinite length direction in 2D materials, p is the specularity parameter which ranges from 0 to 1 and depends on boundary smoothness. $\nu_{\alpha}(\vec{q},p)$is the αcomponent of group velocity along the direction of heat flow.

Considering the fact that the thermal conductivity of graphene and *h*-AlN differ hugely by two orders of magnitude at 300 K [Fig. 3(a)], Fig. 7 shows the dependence of normalized cumulative thermal conductivity on the mean free path (MFP). By checking the MFP for 50% cumulative thermal conductivity, the representative MFP (rMFP) of *h*-AlN are 40.48 and 14.94 nm at 300 and 800 K, respectively, which is lower than graphene (1122.28 nm at 300 K and 183.88 nm at 800 K). It is found that the dominating phonon MFP (and rMFP)are larger at lower temperature [48,49] in both *h*-AlN and graphene. Furthermore, within the temperature range heat in *h*-AlN is carried by phonons with MFP ranging from 1 to 1000 nm which is one order of magnitude lower than graphene (ranging from 10 to 10,000 nm). Thus, for the same feature size, the ballistic effect in graphene is stronger than *h*-AlN due to the larger MFP.

3.5. Electronic origin and lone-pair electrons

Atomic structure and electronic structure are the root cause of phonon thermal transport [45]. To have a top-down understanding of the low thermal conductivity of *h*-AlN, the investigation is not limited to phonon transport characteristics and performance of each phonon branch in the framework of BTE theory, and is further extended to the deepest level effect on low thermal conductivity derived from electronic behavior.

Orbital projected electronic structure of *h*-AlN is shown in Fig. 7(b) for Al atom and Fig. 7(c) for N atom compared with that of graphene in Fig. 7(a). No charge transfer is found in graphene because the bond is formed between the same type of atoms, which is similar to silicene [42]. It is clearly shown in Fig. 7(a) that the *s* orbital is hybridized with

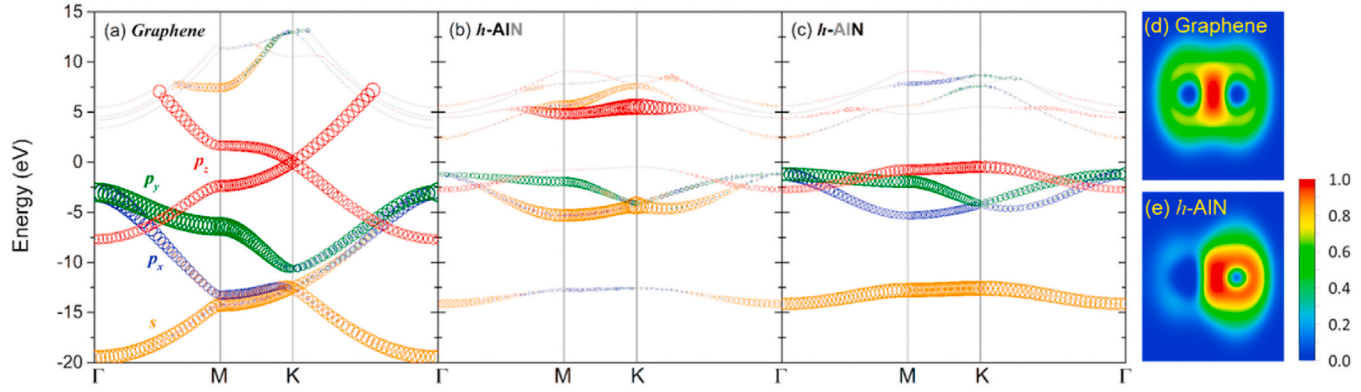

Fig. 7. Orbital projected electronic structures for (a) graphene and (b) Al and (c) N atoms of the *h*-AlN. The band is projected on *s*, p_x, p_y and p_z orbits as shown in orange, blue, green and red bubble, respectively. The electron localization function (ELF) of (d) graphene and (e) *h*-AlN are also plotted for revealing more information on the electronic structures.

the p_x and p_y orbitals and the covalent sp^2 bond is formed between the C atoms in graphene. The p_z orbital near valence band maximum (VBM) is not hybridized with other orbitals at all and forms a large πbond with the p_z orbital of the conduction band, *i.e.*, all the outermost valence electrons (the s^2p^2 valence configuration) participate in the formation of bonding and there are no isolated electrons.

On the contrary, the most striking result as illustrated in Fig. 7(b and c) is that the *s* orbital of N atom in *h*-AlN clearly shows an independent orbital [Fig. 7(c)], which does not contribute to the Al–N bonding. Different from the N atoms, all the *s* and *p* orbitals (p_x, p_y, p_z) of Al atoms participate in the bonding. Thus, the Al-$s/p_x/p_y$ and N-$p_x/p_y/p_z$ jointly contribute to the formation of the Al–N bonds and the s^2 electrons of the s^2p^3 valence configuration from N atoms in *h*-AlN form a pair of isolated electrons, which leads to the asymmetry in orbital evolution. Previous studies have shown that the strong anharmonicity and minimal thermal conductivity of phonon transport in three-dimensional materials is related to lone-pair electrons [46–49], which can be extended to 2D materials and the effect is found closely related to the morphology of lone-pair electrons.

The electron localization function (ELF) of *h*-AlN [Fig. 7(e)] reveals the formation of the lone-pair electrons compared with graphene [Fig. 7(d)]. Pure non-polar covalent bonds are formed between the carbon atoms hybridized by sp^2 [Fig. 7(a)] in graphene, which is due to the fact that there is no charge transfer between the same C atoms. In contrast to graphene [Fig. 7(d)], strong polarization exists in the Al–N bonds, which is even more stronger than the B–N bonds due to the larger electronegativity difference of the Al and N atoms. The polarization in *h*-AlN promotes the bonding electrons being closer to the N atom and thus actively interact with lone-pair electrons. The lone-pair electrons(the s^2 electrons) is observed obviously around the N atoms as shown in Fig. 7(e) by the conspicuous petal-like electron cloud, which is a typical characteristic of the lone pair electrons [49,50]. The isolated s^2 electrons around the N atoms are elecochemically active, which generate strong anharmonic repulsive force by interacting with nearby bonding electrons due to their overlapped wave functions [47]. Slightly different from the three-dimensional structure, in the planar honeycomb-shaped 2D materials like *h*-AlN, lone pair electrons are distributed on both sides of the plane. The special distribution destroys the ring-like bonded electron gas structure in graphene, and thus has a stronger anharmonicity. Moreover, strong polarization emerges in *h*-AlN due to the huge electronegativity difference between Al and N atoms, which brings bonding electrons closer to N atoms. Thus, the interactions of nonlinear repulsive forces between bonding electrons and lone-pair electrons are further strengthened [Fig. 2(b)]. Eventually, an isolated electron pair is formed around the N atom in *h*-AlN, which lead to the strong anharmonicity and low thermal conductivity of *h*-AlN by interacting actively with the bonding electrons forming the Al–N bonds. Besides, the thermal conductivity of *h*-AlN is one order of magnitude lower than that of bulk AlN (321 W/mK) [39], which can be also explained based on the theory of lone-pair electrons. In bulk AlN, all the five outermost electrons of N atom participate in the formation of bonding. In contrast, only three of the five electrons of N atom in monolayer *h*-AlN are bonded with aluminum, *i.e.*, the s^2 electrons in the s^2p^3 valence configuration of N atom do not participate in the bonding. Thus, the non-bonding long-pair electrons arise around N atoms in *h*-AlN, which leads to strong phonon anharmonicity by interacting with the bonding electrons of adjacent atoms (Al). The phenomena reported in previous studies that the thermal conductivity of *h*-GaN is lower than that of bulk GaN can be understood in similar way [40].

The above analysis provides direct evidence for the strong anharmonicity in *h*-AlN as revealed by the representative FA phonon modes. From the series of microscopic picture as described above, the anharmonic repulsive force stems from the asymmetry of orbital hybridization between Al and N atoms in *h*-AlN, which is formed due to non-bonding lone-pair electrons.

4. Conclusion

In summary, by solving phonon BTE based on first-principles calculations, we demonstrate the low thermal conductivity of *h*-AlN (74.43 W/mK) compared with graphene (~3094.98 W/mK). Considering that the FA phonon branch dominates the thermal conductivity in both *h*-AlN and graphene, the conditions for attaining a difference of two orders of magnitude are met by achieving (1) a lower group velocity for *h*-AlN derived from the softened low-frequency acoustic phonon modes, which, however, is not fully responsible for the two orders of magnitude difference in thermal conductivity compared with graphene; (2) a larger scattering rate of FA phonon branch which is driven by both the stronger phonon anharmonicity and the broken symmetry-based selection rule for phonon-phonon scattering. Generally, the physical properties are fundamentally determined by the behavior of electrons and the strong anharmonicity in *h*-AlN can be traced back to the electronic behavior in a specific hybridization due to the coordination environment and electronic configuration of atoms. In addition to the differences observed intuitively in atomic radius and mass, the s^2 electrons in the s^2p^3 valence configuration of the N atoms for *h*-AlN do not participate in the bonding. Thus, an isolated electron pair is formed, which lead to strong anharmonicity and low thermal conductivity by interacting actively with the bonding electrons. We present a fundamental analysis to reveal the mechanism for the low thermal conductivity of *h*-AlN, which provides valuable perspective for analyzing the thermal transport properties of materials with similar configuration as *h*-AlN. With the electronic bandgap in *h*-AlN, it is promising for *h*-AlN to be used as an excellent dielectric substrate for graphene-based electronics. Further studies can

be conducted on the possible manners to enhance the thermal transport in *h*-AlN, and also on the *h*-AlN and graphene heterojunction, which would broad the potential applications of *h*-AlN.

Declaration of competing interest

The authors declare that they have no known competing financial interests or personal relationships that could have appeared to influence the work reported in this paper.

Data availability

Data will be made available on request.

Acknowledgements

This work was supported by the National Key R&D Program of China (No. 2017YFB0406000). H.W. is supported by the National Natural Science Foundation of China (Grant No. 51906097). G.Q. is supported by the Fundamental Research Funds for the Central Universities (Grant No. 531118010471) and the National Natural Science Foundation of China (Grant No. 52006057). Research reported in this publication is also supported in part by the NSF (award number 2030128) and SC EPSCoR/IDeA Program under NSF OIA-1655740 via SC EPSCoR/IDeA SAN 20-SA05. The views, perspective, and content do not necessarily represent the official views of the SC EPSCoR Program nor those of the NSF. The numerical calculations in this paper have been done on the supercomputing system of the National Supercomputing Center in Changsha.

Appendix A. Supplementary data

Supplementary data to this article can be found online at https://doi.org/10.1016/j.ijthermalsci.2020.106772.

References

[1] F. Schwierz, J. Pezoldt, R. Granzner, Two-dimensional materials and their prospects in transistor electronics, Nanoscale 7 (18) (2015) 8261–8283, https://doi.org/10.1039/C5NR01052G.
[2] G. Qin, et al., Resonant bonding driven giant phonon anharmonicity and low thermal conductivity of phosphorene, Phys. Rev. B 94 (16) (Oct. 2016) 165445, https://doi.org/10.1103/PhysRevB.94.165445.
[3] H.O.H. Churchill, P. Jarillo-Herrero, Phosphorus joins the family, Nat. Nanotechnol. 9 (5) (May 2014) 330–331, https://doi.org/10.1038/nnano.2014.85.
[4] G. Qin, et al., Hinge-like structure induced unusual properties of black phosphorus and new strategies to improve the thermoelectric performance, Sci. Rep. 4 (1) (May 2015) 6946, https://doi.org/10.1038/srep06946.
[5] G. Qin, Q.-B. Yan, Z. Qin, S.-Y. Yue, M. Hu, G. Su, Anisotropic intrinsic lattice thermal conductivity of phosphorene from first principles, Phys. Chem. Chem. Phys. 17 (7) (2015) 4854–4858, https://doi.org/10.1039/C4CP04858J.
[6] K.S. Novoselov, Electric field effect in atomically thin carbon films, Science 306 (5696) (Oct. 2004) 666–669, https://doi.org/10.1126/science.1102896.
[7] S. Ghosh, et al., Extremely high thermal conductivity of graphene: prospects for thermal management applications in nanoelectronic circuits, Appl. Phys. Lett. 92 (15) (Apr. 2008) 151911, https://doi.org/10.1063/1.2907977.
[8] K.F. Mak, C. Lee, J. Hone, J. Shan, T.F. Heinz, "Atomically thin MoS 2 : a new direct-gap semiconductor, Phys. Rev. Lett. 105 (13) (Sep. 2010) 136805, https://doi.org/10.1103/PhysRevLett.105.136805.
[9] Q. Peng, W. Ji, S. De, Mechanical properties of the hexagonal boron nitride monolayer: ab initio study, Comput. Mater. Sci. 56 (Apr. 2012) 11–17, https://doi.org/10.1016/j.commatsci.2011.12.029.
[10] A. Nag, K. Raidongia, K.P.S.S. Hembram, R. Datta, U.V. Waghmare, C.N.R. Rao, Graphene analogues of BN: novel synthesis and properties, ACS Nano 4 (3) (Mar. 2010) 1539–1544, https://doi.org/10.1021/nn9018762.
[11] C. Tusche, H.L. Meyerheim, J. Kirschner, Observation of depolarized ZnO(0001) monolayers: formation of unreconstructed planar sheets, Phys. Rev. Lett. 99 (2) (Jul. 2007), 026102, https://doi.org/10.1103/PhysRevLett.99.026102.
[12] C.R. Dean, et al., Boron nitride substrates for high-quality graphene electronics, Nat. Nanotechnol. 5 (10) (Oct. 2010) 722–726, https://doi.org/10.1038/nnano.2010.172.
[13] E.F. de Almeida, F. de Brito Mota, C.M.C. de Castilho, A. Kakanakova-Georgieva, G. K. Gueorguiev, Defects in hexagonal-AlN sheets by first-principles calculations, Eur. Phys. J. B 85 (1) (Jan. 2012) 48, https://doi.org/10.1140/epjb/e2011-20538-6.
[14] L. Zhao, S. Xu, M. Wang, S. Lin, Probing the thermodynamic stability and phonon transport in two-dimensional hexagonal aluminum nitride monolayer, J. Phys. Chem. C 120 (48) (Dec. 2016) 27675–27681, https://doi.org/10.1021/acs.jpcc.6b09706.
[15] P. Tsipas, et al., Evidence for graphite-like hexagonal AlN nanosheets epitaxially grown on single crystal Ag(111), Appl. Phys. Lett. 103 (25) (Dec. 2013) 251605, https://doi.org/10.1063/1.4851239.
[16] V. Mansurov, T. Malin, Yu Galitsyn, K. Zhuravlev, Graphene-like AlN layer formation on (111)Si surface by ammonia molecular beam epitaxy, J. Cryst. Growth 428 (Oct. 2015) 93–97, https://doi.org/10.1016/j.jcrysgro.2015.07.030.
[17] H.L. Zhuang, A.K. Singh, R.G. Hennig, Computational discovery of single-layer III-V materials, Phys. Rev. B 87 (16) (Apr. 2013) 165415, https://doi.org/10.1103/PhysRevB.87.165415.
[18] Y. Dong, et al., Inverse design of two-dimensional graphene/h-BN hybrids by a regressional and conditional GAN, Carbon 169 (Nov. 2020) 9–16, https://doi.org/10.1016/j.carbon.2020.07.013.
[19] Y. Dong, C. Wu, C. Zhang, Y. Liu, J. Cheng, J. Lin, Bandgap prediction by deep learning in configurationally hybridized graphene and boron nitride, npj Comput Mater 5 (1) (Dec. 2019) 26, https://doi.org/10.1038/s41524-019-0165-4.
[20] M. Yamawaki, M. Ohnishi, S. Ju, J. Shiomi, Multifunctional structural design of graphene thermoelectrics by Bayesian optimization, Sci. Adv. 4 (6) (Jun. 2018) eaar4192, https://doi.org/10.1126/sciadv.aar4192.
[21] M. Wuttig, N. Yamada, Phase-change materials for rewriteable data storage, Nat. Mater. 6 (11) (2007) 824–832.
[22] T. Siegrist, P. Merkelbach, M. Wuttig, Phase change materials: challenges on the path to a universal storage device, Annual Review of Condensed Matter Physics 3 (1) (2012) 215–237, https://doi.org/10.1146/annurev-conmatphys-020911-125105.
[23] J.-Y. Raty, C. Otjacques, R. Peköz, V. Lordi, C. Bichara, Amorphous phase change materials: structure, stability and relation with their crystalline phase, in: C. Massobrio, J. Du, M. Bernasconi, P.S. Salmon (Eds.), In *Molecular Dynamics Simulations of Disordered Materials: from Network Glasses to Phase-Change Memory Alloys*, Springer International Publishing, Cham, 2015, pp. 485–509.
[24] D.R. Clarke, M. Oechsner, N.P. Padture, Thermal-barrier coatings for more efficient gas-turbine engines, MRS Bull. 37 (10) (Oct. 2012) 891–898, https://doi.org/10.1557/mrs.2012.232.
[25] Y. Zhao, et al., Porous architecture and thermal properties of thermal barrier coatings deposited by suspension plasma spray, Surf. Coating. Technol. 386 (Mar. 2020) 125462, https://doi.org/10.1016/j.surfcoat.2020.125462.
[26] G. Kresse, J. "Hafner, Ab inito molecular dynamics for metals, Phys. Rev. B 47 (1993) 558–561.
[27] G. Kresse, J. Furthmüller, "'Efficient iterative schemes for ab initio total-energy calculations using a plane-wave basis set, Phys. Rev. B 54 (1996) 11169–11186.
[28] G. Kresse, J. Hafner, "*Ab initio* molecular-dynamics simulation of the liquid-metal–amorphous-semiconductor transition in germanium, Phys. Rev. B 49 (20) (May 1994) 14251–14269, https://doi.org/10.1103/PhysRevB.49.14251.
[29] H.J. Monkhorst, J.D. Pack, Special points for Brillouin-zone integrations, Phys. Rev. B 13 (12) (Jun. 1976) 5188–5192, https://doi.org/10.1103/PhysRevB.13.5188.
[30] A. Togo, F. Oba, I. Tanaka, First-principles calculations of the ferroelastic transition between rutile-type and CaCl 2 -type SiO 2 at high pressures, Phys. Rev. B 78 (13) (Oct. 2008) 134106, https://doi.org/10.1103/PhysRevB.78.134106.
[31] W. Li, L. Lindsay, D.A. Broido, D.A. Stewart, N. Mingo, "Thermal conductivity of bulk and nanowire Mg 2 Si x Sn 1 − x alloys from first principles, Phys. Rev. B 86 (17) (Nov. 2012) 174307, https://doi.org/10.1103/PhysRevB.86.174307.
[32] W. Li, J. Carrete, N.A. Katcho, N. Mingo, " ShengBTE, A solver of the Boltzmann transport equation for phonons, Comput. Phys. Commun. 185 (6) (Jun. 2014) 1747–1758, https://doi.org/10.1016/j.cpc.2014.02.015.
[33] M. Omini, A. Sparavigna, Beyond the isotropic-model approximation in the theory of thermal conductivity, Phys. Rev. B 53 (14) (Apr. 1996) 9064–9073, https://doi.org/10.1103/PhysRevB.53.9064.
[34] A. Ward, D.A. Broido, Intrinsic phonon relaxation times from first-principles studies of the thermal conductivities of Si and Ge, Phys. Rev. B 81 (8) (Feb. 2010), 085205, https://doi.org/10.1103/PhysRevB.81.085205.
[35] L. Lindsay, D.A. Broido, Three-phonon phase space and lattice thermal conductivity in semiconductors, J. Phys. Condens. Matter 20 (16) (Apr. 2008) 165209, https://doi.org/10.1088/0953-8984/20/16/165209.
[36] C. Chang, L.-D. Zhao, Anharmoncity and low thermal conductivity in thermoelectrics, Materials Today Physics 4 (Mar. 2018) 50–57, https://doi.org/10.1016/j.mtphys.2018.02.005.
[37] Q. Cai, et al., High thermal conductivity of high-quality monolayer boron nitride and its thermal expansion, Sci. Adv. 5 (6) (Jun. 2019) eaav0129, https://doi.org/10.1126/sciadv.aav0129.
[38] G. Qin, Z. Qin, H. Wang, M. Hu, Anomalously temperature-dependent thermal conductivity of monolayer GaN with large deviations from the traditional 1/T law,, Phys. Rev. B 95 (19) (May 2017) 195416, https://doi.org/10.1103/PhysRevB.95.195416.
[39] J.H. Seol, et al., Two-dimensional phonon transport in supported graphene, Science 328 (5975) (Apr. 2010) 213–216, https://doi.org/10.1126/science.1184014.
[40] X. Gu, R. Yang, First-principles prediction of phononic thermal conductivity of silicene: a comparison with graphene, J. Appl. Phys. 117 (2) (Jan. 2015), 025102, https://doi.org/10.1063/1.4905540.
[41] H. Wang, G. Qin, G. Li, Q. Wang, M. Hu, Low thermal conductivity of monolayer ZnO and its anomalous temperature dependence, Phys. Chem. Chem. Phys. 19 (20) (2017) 12882–12889, https://doi.org/10.1039/C7CP00460E.

[42] L. Lindsay, D.A. Broido, N. Mingo, Flexural phonons and thermal transport in graphene, Phys. Rev. B 82 (11) (Sep. 2010) 115427, https://doi.org/10.1103/PhysRevB.82.115427.
[43] Z. Cheng, et al., Experimental observation of high intrinsic thermal conductivity of AlN, Phys. Rev. Materials 4 (4) (Apr. 2020), 044602, https://doi.org/10.1103/PhysRevMaterials.4.044602.
[44] Y. Jiang, S. Cai, Y. Tao, Z. Wei, K. Bi, Y. Chen, Phonon transport properties of bulk and monolayer GaN from first-principles calculations, Comput. Mater. Sci. 138 (Oct. 2017) 419–425, https://doi.org/10.1016/j.commatsci.2017.07.012.
[45] Z. Qin, G. Qin, X. Zuo, Z. Xiong, M. Hu, Orbitally driven low thermal conductivity of monolayer gallium nitride (GaN) with planar honeycomb structure: a comparative study, Nanoscale 9 (12) (2017) 4295–4309, https://doi.org/10.1039/C7NR01271C.
[48] Y. Dong, A.R. Khabibullin, K. Wei, J.R. Salvador, G.S. Nolas, L.M. Woods, "Bournonite $PbCuSbS_3$: stereochemically active lone-pair electrons that induce low thermal conductivity, ChemPhysChem 16 (15) (Oct. 2015) 3264–3270, https://doi.org/10.1002/cphc.201500476.
[46] X. Wang, F. Liebau, Studies on bond and atomic valences. I. correlation between bond valence and bond angles in SbIII chalcogen compounds: the influence of lone-electron pairs, Acta Crystallogr B Struct Sci 52 (1) (Feb. 1996) 7–15, https://doi.org/10.1107/S0108768195004472.
[47] E.J. Skoug, D.T. Morelli, Role of lone-pair electrons in producing minimum thermal conductivity in nitrogen-group chalcogenide compounds, Phys. Rev. Lett. 107 (23) (2011) 235901.
[49] D.T. Morelli, V. Jovovic, J.P. Heremans, "Intrinsically minimal thermal conductivity in cubic I $-V-VI_2$ semiconductors, Phys. Rev. Lett. 101 (3) (Jul. 2008), 035901, https://doi.org/10.1103/PhysRevLett.101.035901.
[50] D.B. Chesnut, An electron localization function study of the lone pair, J. Phys. Chem. 104 (49) (Dec. 2000) 11644–11650, https://doi.org/10.1021/jp002957u.